# A complicated Duffing oscillator in the surface-electrode ion trap

**Hao-Yu Wu · Yi Xie · Wei Wan · Liang Chen ·
Fei Zhou · Mang Feng**

**Abstract** The oscillation coupling and different nonlinear effects are observed in a single trapped $^{40}Ca^+$ ion confined in our home-built surface-electrode trap (SET). The coupling and the nonlinearity are originated from the high-order multipole potentials, such as hexapole and octopole potentials, due to different layouts and the fabrication asymmetry of the SET. We solve a complicated Duffing equation with coupled oscillation terms by the multiple-scale method, which fits the experimental values very well. Our investigation in the SET helps for exploring multi-dimensional nonlinearity using currently available techniques and for suppressing instability of qubits in quantum information processing with trapped ions.

## 1 Introduction

The Duffing oscillator is generally used to describe nonlinear dynamics in oscillating systems [1–4]. The corresponding Duffing equation models a damping and driven oscillator with more complicated behavior than simple harmonic motion, which can be used to exhibit chaos in dynamics and hysteresis in resonance [5–10].

H.-Y. Wu · Y. Xie · W. Wan · L. Chen (✉) · F. Zhou ·
M. Feng (✉)
State Key Laboratory of Magnetic Resonance and Atomic and
Molecular Physics, Wuhan Institute of Physics and Mathematics,
Chinese Academy of Sciences, Wuhan 430071, China
e-mail: liangchen@wipm.ac.cn

M. Feng
e-mail: mangfeng@wipm.ac.cn

H.-Y. Wu · Y. Xie · W. Wan
University of the Chinese Academy of Sciences, Beijing 100049,
China

On the other hand, the motion of trapped ions is highly controllable and can be employed to transfer quantum information when cooled down to ground state [11]. Since it is effectively approximated to be harmonic, the ion motion in a quadruple electromagnetic trap [12] can be regarded as a good mechanical oscillator, which may exhibit nonlinearity when driven to the nonlinear field. For example, Duffing nonlinear dynamics have been investigated in a single ion confined in the linear ion trap [13]. The trap nonlinearity introduces instability in the motion of the ion, which should be avoided in most times, but can also be used in resonance rejection and parameter detection in mass spectrometry [14, 15]. Recent research also showed the feasibility of phonon lasers based on the nonlinearity of a single trapped ion under laser irradiation [16, 17].

We focus in this work on the nonlinearity and coupled motion in a home-built surface-electrode trap (SET). The SET, with capability to localize and transport trapped ions in different potential wells, is a promising setup for large-scale quantum information processing [18]. In comparison with conventional linear Paul traps, however, the reduced size and asymmetry in SET lead to stronger hexapole and octopole potentials [19–21], which affect the stability of the ion trapping. To solve the problem, we have to understand the source and the strength of the nonlinearity in multi-dimensional cases. Due to complexity resulted from the hexapole and octopole potentials, the ion's oscillation in the SET cannot be simply described by the Duffing oscillator as in the linear trap, but can be described by an inhomogeneous-coupled Duffing oscillator involving quadratic and cubic nonlinearities in the restoring force. We observed the nonlinearity in our SET, and derived by the method of multiple scales an inhomogeneous-coupled Duffing oscillator to fit the experimental values, which shows that both the nonlinearity and axial–radial coupling

exist in the case of the frequency resonance (i.e., around the regime of zero driving detuning or/and meeting the frequency commensurate relation). Moreover, we show in the noncoupling case different nonlinear effects in different dimensions, which is due to different asymmetry in fabrication of the SET.

## 2 Experimental setup and images of ion motion

Our home-built SET is a 500 μm-scaled planar trap with five electrodes for radial confinement and fabricated by printed circuit board technology [22]. As shown in Fig. 1, the five electrodes consist of a central electrode, two radio-frequency (RF) electrodes and two outer segmented dc electrodes, where the RF electrodes, the central electrode and the gaps in between are of the same width of 500 μm. Each outer segmented electrode consists of five component electrodes, i.e., a middle electrode, two control electrodes and two end electrodes. The widths of the control electrodes and end electrodes in the segment are 1.5 mm, and the middle electrode is 1 mm wide. The gap in the segmented electrode is of 500 μm width. The electrodes are made of copper on a vacuum-compatible printed circuit board substrate. The radial confinement potential is produced by the RF voltage with the amplitude $U \sim 400$ V (0-Peak), and RF $\Omega = 2\pi \times 15$ MHz applied on the RF electrodes. The axially confining potential is produced by an end-cap (EC) voltage $V_{ec} = 40$ V applied on the EC electrodes, with zero voltage on other electrodes. When the SET works, the trapped $^{40}Ca^+$ ion stands above the electrodes by 0.8 mm, and the pseudopotential trapping depth is below 1 eV.

The experimental setup is plotted in Fig. 2, where the ultraviolet radiation at 397 nm excites $4s^2S_{1/2} - 4p^2P_{1/2}$
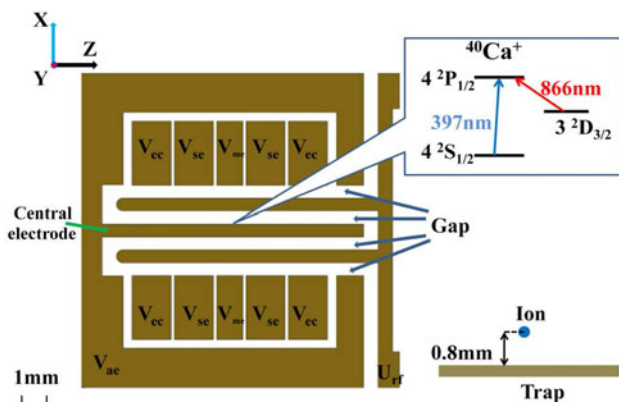
transition by a grating-stabilized laser diode with power up to 30 mW and linewidth less than 2 MHz. Another grating-stabilized laser diode at 866 nm with power up to 100 mW and linewidth less than 5 MHz excites the $3d^2D_{3/2} - 4p^2P_{1/2}$ transition. The frequencies of both the laser diodes have been calibrated to the wavelength meter (HighFiness, WS-7). Typical laser powers at the trap center are 50 μW for 397 nm in red detuning ($-80$ MHz in most implementations of our experiment, see explanation later) and 500 μW for 866 nm in carrier transition. In our experiment, the laser beams are directed in parallel with the trap surface (i.e., $xz$ plane) with an angle of 5 degrees with respect to the trap axis. The single $^{40}Ca^+$ ion is laser cooled and stably confined in the SET, which is monitored by photon scattering collected by an electron-multiplying charge-coupled-device (EMCCD) camera and a photo-multiplier tube (PMT). Outside the vacuum chamber, the electrical connections immediately encounter a "filter box," which provides low-pass filtering of the voltages applied to the electrodes. An additional drive force is electrically connected to one of the middle electrodes behind the filter box, which provides an excitation to drive the ion away from equilibrium. Due to the design of our SET system, the motion of the ion is detected only in the $xz$ plane by the EMCCD. As a result, what we study throughout the work is the oscillation only along the axial direction ($z$ axis) and the radial direction ($x$ axis), whose harmonic frequencies are, respectively, $\omega_{0z}/2\pi = 191.7$ kHz and $\omega_{0x}/2\pi = 425$ kHz in the linear regime of the trap. Moreover, since the harmonic frequency in $y$ axis is $\omega_{0y}/2\pi = 925$ kHz, much bigger than in other axes, the ion can be regarded as a very tight confinement in $y$ direction. We have suppressed the micro-motion by the RF-photon cross-correlation compensation [23], which yields cooling of the ion down to the temperature below 10 mK.



Fig. 1 The layout of our home-built SET with the *top-right* inset for the relevant energy levels of the trapped $^{40}Ca^+$ ion. The $^{40}Ca^+$ ion is cooled by the laser beam at 397 nm on the $4s^2S_{1/2} - 4p^2P_{1/2}$ transition, helped by another laser light at 866 nm as repumping. Here, the trapped ion is above the electrodes by 0.8 mm (See the *bottom-right* inset)
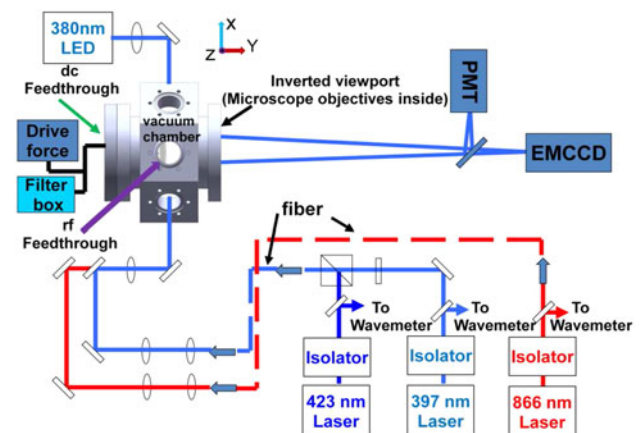


Fig. 2 Schematic of our experimental setup. The main components are explained in the text

To study the nonlinear mechanical response, we drive the ion to the nonlinear regime by a small oscillating voltage, i.e., $V = 7$ V, applied on one of the middle electrodes. We slowly increase the driving frequency with the scan step 0.1 kHz, from 189.0 to 433.0 kHz (the positive scan), and the ion oscillates first along the $z$ axis and then turns to the $x$ axis for oscillation. The particularly interesting observation is the simultaneous responses, i.e., a rectangle trajectory, in both $x$ and $z$ axes when the sweep is close to the harmonic resonator frequency in either of the axes. Similar behavior is also found in the negative scan.

We measure the ion oscillation by taking time-averaged images from the EMCCD. In Fig. 3, seventeen such images for different drive frequencies are presented for positive and negative scans, respectively. For the ion originally oscillating in the $z$ axis, we slowly scan the drive frequency $\omega_z$ across the harmonic resonance at $\omega_{0z}$. When the detuning $\sigma$ approaches zero, the rectangle trajectory appears, implying a coupled motion between $x$ and $z$ axes due to axial–radial coupling (explained later). For a more clarified observation, we scan with smaller steps around the regime $\sigma = 0$, as shown in Fig. 4 which gives us an accurate range from the appearance of the rectangle to the disappearance. Moreover, from the ninth image in Fig. 4, the amplitude in $x$ axis turns to be larger than in the $z$ axis, which is beyond the energy (i.e., phonon) transferred from the $z$ axis. The energy excluding that from the coupled motion is due to heating of the laser, which is relevant to the detuning of the laser irradiation. For our purpose, we only focus our attention on the production and transfer of the phonons by driving. So we fix the laser detuning in our experimental implementation, which gives a weak constant heating on the ion and can be treated effectively as a constant factor. In addition, no feedback of the vibrational effect is observed from the $x$ axis to the $z$ axis during the period of motion coupling.

## 3 Theoretical model

To understand the observation above, we have to consider the multipole potential in the SET, which is given by [24]

$$\phi_i(x, y, z) = \sum_{j=1}^{\infty} g_{ij} M_j Y_j(x, y, z), \tag{1}$$

where the subscript $i$ labels different electrodes and the subscript $j$ is for the spherical harmonics $Y_j(x, y, z)$. Both $Y_j(x, y, z)$ and the related parameters $M_j$ are defined in [24]. $g_{ij}$ is the weight factor for different electrodes. In this treatment, the initial equilibrium position of the single trapped ion is defined as the origin of the coordinates. The five-wire SET generally consists of quadrupole and
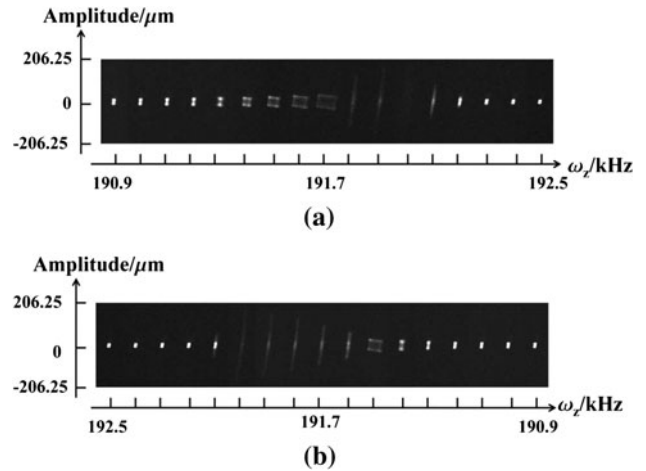


**Fig. 3** Time-averaged images of a single trapped ion taken at different drive frequencies, with (**a**) the positive scan and (**b**) the negative scan. The prime oscillation is along the axial direction, and the scan step is 0.1 kHz. The *rectangles* appear in the images at resonance frequency due to axial–radial coupling
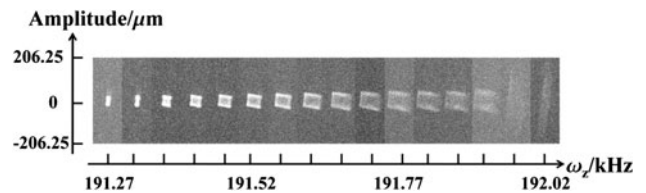


**Fig. 4** The coupled oscillation in the time-averaged images for the positive scan. Comparing to Fig. 3, the scan with smaller step (0.01 kHz) presents clearer pictures for the *rectangle trajectories* from appearance to disappearance, where 16 images are selected here in series with the frequency step 0.05 kHz

hexapole potentials [21]. Considering the asymmetry in our SET, we also involve octopole potential in our treatment. Following the definition in [24], we have the subscripts $j = 5, \ldots, 25$ where $j$ from 5 to 9, from 10 to 16 and from 17 to 25 correspond, respectively, to the quadrupole, hexapole and octopole potentials. For different potentials $\Psi_i = V_i + U_i \cos(\Omega t)$ applied, respectively, to $N$ electrodes, where $V_i$ is the dc voltage on the electrode $i$ and $U_i \cos(\Omega t)$ represents the RF voltage $U_i$ on the electrode $i$ driven at frequency $\Omega$, we rewrite Eq. (1) for the dc potential $\Phi_{dc}$ and the RF potential $\Phi_{RF}$ as

$$\Phi_{dc}(x, y, z) = \sum_{j=5}^{25} V_j^* M_j Y_j(x, y, z),$$

$$\Phi_{RF}(x, y, z) = \sum_{j=5}^{25} U_j^* \cos(\Omega t) M_j Y_j(x, y, z), \tag{2}$$

where we have used $U_j^* = \sum_{i=1}^{N} U_i g_{ij}$ and $V_j^* = \sum_{i=1}^{N} V_i g_{ij}$.

Moreover, we have the 1D motional equation for the trapped ion [25],

$$\frac{d^2\xi}{dt^2} + 2\mu\frac{d\xi}{dt} + \frac{e}{m}\frac{\partial \Phi_{dc}}{\partial \xi} + \frac{e^2}{2m^2}\frac{\partial}{\partial \xi}\left(\left\langle \left| \int \frac{\partial \Phi_{RF}}{\partial \xi} dt \right|^2 \right\rangle\right)$$
$$= k_\xi \cos(\omega_\xi t), \tag{3}$$

with $\xi = x$, $y$ and $z$. Combining Eq. (2) with Eq. (3), we obtain the equation of motion in the $z$ direction,

$$\frac{d^2z}{dt^2} + 2\mu\frac{dz}{dt} + \omega_{0z}^2 z + \alpha_2 z^2 + \alpha_3 z^3 + \alpha_{21}z^2 y + \alpha_{22}z^2 x$$
$$+ \alpha_4 zy^2 + \alpha_5 zx^2 + \alpha_6 zxy + \alpha_7 zy + \alpha_8 zx = k_z \cos(\omega_z t), \tag{4}$$

where $x$, $y$ and $z$ represent, respectively, the displacement of the ion from the equilibrium position in the three dimensions, $\mu$ is the linear damping parameter originated from the recoil due to photon absorption, $k_z$ is the driving amplitude. The detailed expressions of the nonlinear coefficients $\alpha_i$ ($i = 2, 21, 22, 3, 4, 5, 6, 7, 8$) can be found in "Appendix 1." Compared to the Duffing oscillator in [13], Eq. (4) is a complicated Duffing oscillator, containing additional coupled motion terms.

The reason we concentrate on the motion in $z$ axis lies in our intention to study the production and transfer of the phonons due to driving, independent from the laser heating. For the fixed laser detuning in our implementation, the laser heating in $z$ axis is much less than in $x$ axis. Moreover, in this case, there is no feedback of the laser effect on the $z$ axis from the $x$ direction during the period of the coupled motion. As a result, we may consider the laser effect on the motion in $z$ axis as an effective constant. In contrast, the laser effect on the $x$ axis is strong and varied with time, which makes the problem much more complicated. Also due to this reason, when we consider the motional effect from $x$ and $y$ axes to $z$ axis due to the coupled motion, we simply solve the equation of motion in $z$ axis by involving the zeroth order and first order of solutions in $x$ and $y$ axes, which present negligible effects from laser heating (see Eqs. (20)–(26) in "Appendix 2"). Using the method of multiple scales [26], we obtain the steady-state solution to Eq. (4) as

$$\sigma = \frac{3a^2}{8\omega_{0z}}\left(\alpha_3 + \frac{-10\alpha_2^2}{9\omega_{0z}^2} + \frac{-2\alpha_8\alpha_{2x}c^2}{3\omega_{0x}^2 a^2} + \frac{-2\alpha_7\alpha_{2y}b^2}{3\omega_{0y}^2 a^2}\right.$$
$$\left. + \frac{2\alpha_4 b^2}{3a^2} + \frac{2\alpha_5 c^2}{3a^2}\right) \pm \sqrt{\frac{k_z^2}{4\omega_{0z}^2 a^2} - \mu^2}, \tag{5}$$

where the nonlinear coefficients $\alpha_{2x}$ and $\alpha_{2y}$ are relevant to the coupled motion equations along $x$ and $y$ axes. $c$, $b$ and $a$ are the response amplitudes, respectively, in $x$, $y$ and $z$ directions. $\omega_{0x}/2\pi$ and $\omega_{0y}/2\pi$ represent the harmonic frequencies in $x$ and $y$ axes. For more clarification, we define a parameter $\alpha_{total}$ as

$$\alpha_{total} = \alpha_3 + \Delta\alpha_2 + \Delta\alpha, \tag{6}$$

where $\alpha_3$ originates from the cubic nonlinearity, $\Delta\alpha_2 = \frac{-10\alpha_2^2}{9\omega_{0z}^2}$ represents the nonlinear coefficient that comes from quadric nonlinearity, and $\Delta\alpha = \frac{-2\alpha_8\alpha_{2x}c^2}{3\omega_{0x}^2 a^2} + \frac{-2\alpha_7\alpha_{2y}b^2}{3\omega_{0y}^2 a^2} + \frac{2\alpha_4 b^2}{3a^2} + \frac{2\alpha_5 c^2}{3a^2}$ corresponds to the nonlinear dispersion relevant to the coupled motion. Substituting $\alpha_{total}$ into Eq. (5), we obtain

$$\sigma = \frac{3\alpha_{total}}{8\omega_{0z}}a^2 \pm \sqrt{\frac{k_z^2}{4\omega_{0z}^2 a^2} - \mu^2}. \tag{7}$$

## 4 Discussion about the nonlinearity and coupling

In our home-built SET, since the harmonic frequency in $y$ axis is much bigger than in other axes, the ion is confined very tightly in $y$ direction, which leads to a reasonable assumption $b/a \ll 1$. As a result, the coupled term $\Delta\alpha$ is reduced to $\Delta\alpha = \chi c^2/a^2$ with $\chi = \frac{-2\alpha_8\alpha_{2x}}{3\omega_{0x}^2} + \frac{2\alpha_5}{3}$.

Moreover, $\alpha_3$ and $\Delta\alpha_2$ in Eq. (6) are nothing to do with the coupled motion and their sum $\alpha_3 + \Delta\alpha_2$ can be measured experimentally by

$$a_m = \sqrt{\frac{8\omega_{0z}\sigma_m}{3(\alpha_3 + \Delta\alpha_2)}}, \tag{8}$$

with the maximal amplitude $a_m$ and the maximal detuning $\sigma_m$ in the noncoupling case. As a result, Eq. (7) is reduced to a steady-state solution to the amplitude of the response $a$ with respect to the driving detuning $\sigma$ for the known driving force amplitude $k_z$,

$$\sigma = \frac{3a^2}{8\omega_{0z}}\left(\alpha_3 + \Delta\alpha_2 + \chi\frac{c^2}{a^2}\right) \pm \sqrt{\frac{k_z^2}{4\omega_{0z}^2 a^2} - \mu^2}. \tag{9}$$

In our experiment, $\omega_{0z}$ is measured via ion response in the linear regime, $k_z = 0.075 \times 10^6$ Hz$^2$ m is obtained by observing the ion displacement versus the middle electrode voltage [20], $\alpha_3 + \Delta\alpha_2 = 0.1959 \times 10^{18}$ Hz$^2$/m$^2$ is measured using the observed dependence of $a_m$ on the maximal detuning $\sigma_m$. We evaluate $\mu = 177.1$ Hz using the relation $a_m = k_z/(2\mu\omega_{0z})$. The comparison in the noncoupling case between the measured and calculated values of $a$ and $\sigma$ is made in Fig. 5a, where Eq. (9) without the coupling term $\Delta\alpha$ (the black solid curve) can fit most experimental values for both the positive and negative scans (red stars and green crosses, respectively). In this situation, the vibrational amplitude $c$ in $x$ axis is negligible. Some experimental values around $\sigma = 0$, which are not fitted well by the solid curve, are actually relevant to the case of the coupled motion. To be more clarified, we scan the region around $\sigma = 0$ with smaller step than in Fig. 5a. The fitting by considering the coupling term $\Delta\alpha$ in our calculation can
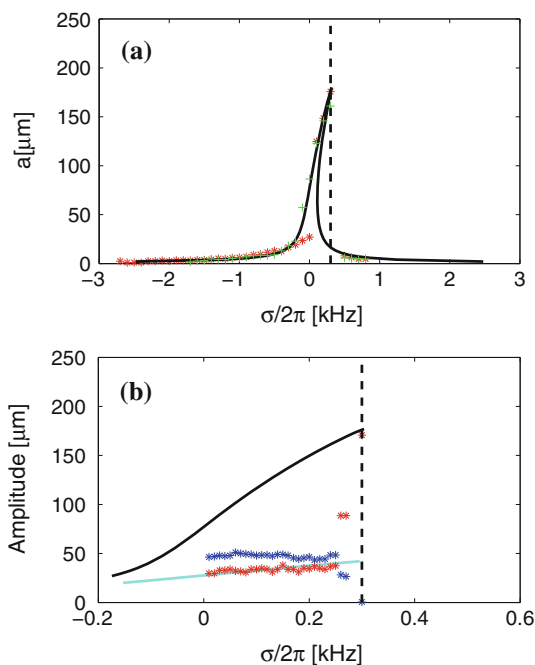
**Fig. 5** The measured and calculated amplitudes with respect to the driving detuning, where the *black dashed lines* indicate the detunings for maximal amplitudes of oscillations. **a** The measured values correspond to the situation in Fig. (3). Calculation (*black solid curve*) by Eq. (9) without the coupling term fits most of the measured values with positive scan (*red stars*) and negative scan (green crosses). The scan step is 0.1 kHz. **b** The measured values correspond to the situation in Fig. (4). Calculation (*light blue solid line*) by Eq. (9) with the coupling term fits the measured values with positive slow scan (*red stars*) around zero detuning. The scan step is 0.01 kHz, and the *blue stars* are for the measured values of the vibrational amplitude $c$ in $x$ axis. As a comparison, the calculation without the coupling term is plotted (the *black solid curve*)

fully cover the measured data, as shown in Fig. 5b. In such a case, we find that the vibrational amplitude $c$ in $x$ axis is visible, which is excited by the energy transfer from $z$ axis due to motional coupling. This energy transferred from $z$ to $x$ axis is nearly constant in the adiabatic operation so that we obtain $\chi \frac{c^2}{a^2} \approx 4.5 \times 10^{18} \text{Hz}^2/\text{m}^2$.[1] Figure 5b also shows that the motional coupling stops when $\sigma$ approaches 0.25 kHz. We see that $a$ goes up to the maximum with $c$ dropping to zero, implying that the system returns to the noncoupling case. Therefore, the vibrational trajectories imaged in Figs. 3 and 4 can be fully understood by the complicated Duffing oscillator with and without the term for the coupled motion.

The intra-dimensional coupling of motion depends on the frequency commensurate relation between $x$ and $z$ axes, which in our case of coupling, we have $\omega'_{0x} \approx 2\omega'_{0z}$ with

---

[1] This is a rough estimate for the measured values (i.e., the blue stars) which are nearly constant. The blue stars higher than the red stars mean the fact that laser heating is involved. As a result, for a careful understanding, it needs a serious solution to the 3D euqations of motion of the system.
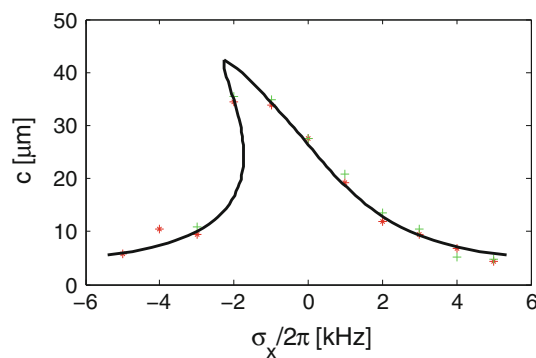


**Fig. 6** The measured and calculated amplitudes in $x$ axis with respect to the driving detuning, where the scan step is 1 kHz and the measurement is made in the no-coupling case. Calculation (*black solid curve*) fits most of the measured values with positive scan (*red stars*) and negative scan (*green crosses*). $\sigma_x$ is the driving detuning in the $x$ direction

$\omega'_{0x}$ and $\omega'_{0z}$ being instantaneous frequencies in $x$ and $z$ axes, respectively. These instantaneous frequencies are slightly different from the secular frequencies $\omega_{0x}$ and $\omega_{0z}$ measured in the linear regime, due to the frequency shifts with the variation of the oscillating amplitudes in the nonlinear regime of the ion trap [25]. Moreover, in our theoretical treatment, the shifts of the secular frequencies can be effectively collected into the complex amplitudes, such as the terms of $A$, $B$ and $C$ (defined in the "Appendix 2"), and thereby have no affect on the final result.

Moreover, we have also checked nonlinear effects in a different direction in our SET by applying the drive on the $x$ axis and repeating the experimental steps as above for $z$ axis. To this end, we modify the laser detuning to make sure a weak heating on the motion along $x$ axis. Under the assumption that the laser heating is effectively considered as a constant, the behavior can be described by a slight modification of Eq. (4) by exchanging $z$ and $x$, and replacing $k_z$ and $\omega_z$ by $k_x$ and $\omega_x$. As an example, we only present the noncoupling case in Fig. 6, where the measured data are fitted well by the steady solution to the complicated Duffing oscillator with different nonlinear coefficients and different damping rates from in Fig. 5a. In comparison with the shape of the curve in Fig. 5a, the oscillation in such a case reaches the maximal amplitude before $\sigma_x = 0$, i.e, the red detuning, corresponding to $\alpha_3 + \Delta\alpha_2 < 0$ in Eq. (8). This implies negative coefficients of quadratic and cubic terms in Eq. (4) originated from the different asymmetry from in $z$ axis.

## 5 Conclusion

In conclusion, we have experimentally investigated the complicated oscillations in our home-built SET, which are

related to the hexapole and octopole potentials. Both the coupling and noncoupling cases, as well as the driving along different axes, are studied. Our observation can be fully understood by the nonlinear effects and the motional coupling from the solution of a complicated Duffing oscillator.

In comparison with the relevant study on a single ion oscillating in the linear trap [13], our home-made SET owns stronger hexapole and octopole potentials, which cause more fruitful nonlinear effects and even the motional coupling between different directions. Although there are also axial–radial couplings observed in linear trap, e.g., with ion cloud in [27], such a motional coupling is much more evident in the SET, which, in addition to the couplings regarding $zx$ and $xz^2$, is also reflected in the $zx^2$ term in Eq. (4) with the coefficient $\alpha_5$. According to our calculation, the motional coupling in our observation is mainly influenced by the coefficients $\alpha_5$ and $\alpha_8$, which implies the combined action from the stronger quadrupole, hexapole and octopole potentials. This might be the reason that the rectangle trajectories have never been observed previously in linear ion traps. Moreover, in Figs. 3, 4 and 5, the vibration in $x$ direction is not seriously treated in this work, because it is subject to potential nonlinearity, the coupled motion and the strong laser heating, which is much more complicated than in $z$ axis. As a result, even for the observed values in Fig 5b under adiabatic operation, we have just made a simple fitting, instead of a full solution to 3D equations of motion. The strong laser heating yields time-dependent damping, varying between positive and negative values corresponding, respectively, to the heating and cooling. It is difficult to have analytical discussion for such a case, but it might involve more interesting physics. The work in this respect is under our investigation.

Furthermore, recent investigation of the phonon laser based on the nonlinear oscillation of the trapped ion demonstrated the analogy to the Fabry–Perot laser with 100 % reflecting mirrors [16, 17]. In contrast, the SET under our study seems an asymmetry Fabry–Perot cavity, which may yield two split beams of the phonon laser in perpendicular axes. Coherent transfer between the two split phonon beams would be useful in fundamental physics and practical application. Further work in this aspect is underway.

With the trapped ions cooled down to the motional ground state, we may have an excellent platform to demonstrate nonlinear behavior in a fully quantum mechanical regime and also carry out quantum logic gate operations. Therefore, our work presents a way to exploring complicated nonlinearity using experimentally available techniques, and it is also useful for suppressing detrimental effects from the nonlinearity in quantum information processing using trapped ions.

## Appendix 1: The nonlinear coefficients in Eq. (4)

Our calculation is based on Eq. (4), in which the nonlinear coefficients originate from the hexapole and octopole potentials. By setting $e$ and $m$ to be the electric quantity and the mass of a single calcium ion, we have the nonlinear coefficients as

$$\alpha_3 = \frac{36e^2 r_0^2 (U_{13}^*)^2 M_{13}^2}{m^2 r_0^8 \Omega^2} + \frac{140 e M_{21} [m r_0^4 (V_{21}^*) \Omega^2 + 8 e r_0^2 (U_{21}^*)(U_7^*) M_7]}{m^2 r_0^8 \Omega^2},$$
(10)

$$\alpha_2 = \frac{6 e r_0 M_{13} [m r_0^4 (V_{13}^*) \Omega^2 + 6 e r_0^2 (U_7^*)(U_{13}^*) M_7]}{m^2 r_0^8 \Omega^2}, \quad (11)$$

$$\alpha_{21} = \frac{3e [70 e r_0^2 M_6 M_{21} (U_6^*)(U_{21}^*) + 42 e r_0^2 M_7 M_{20} (U_7^*)(U_{20}^*)]}{m^2 r_0^8 \Omega^2} + \frac{3e [24 e r_0^2 M_{12} M_{13} (U_{12}^*)(U_{13}^*) + 7 m r_0^4 \Omega^2 M_{20} (V_{20}^*)]}{m^2 r_0^8 \Omega^2},$$
(12)

$$\alpha_{22} = \frac{3e [70 e r_0^2 M_8 M_{21} (U_8^*)(U_{21}^*) + 42 e r_0^2 M_7 M_{22} (U_7^*)(U_{22}^*)]}{m^2 r_0^8 \Omega^2} + \frac{3e [24 e r_0^2 M_{13} M_{14} (U_{13}^*)(U_{14}^*) + 7 m r_0^4 \Omega^2 M_{22} (V_{22}^*)]}{m^2 r_0^8 \Omega^2},$$
(13)

$$\alpha_4 = \frac{e [32 e r_0^2 (U_{12}^*)^2 M_{12}^2 - 18 e r_0^2 (U_{13}^*)^2 M_{13}^2 - 6 e r_0^2 (U_{13}^*)(U_{15}^*) M_{13} M_{15} + 21 e r_0^2 (U_6^*)(U_{20}^*) M_6 M_{20}]}{m^2 r_0^8 \Omega^2} + \frac{e [-60 m r_0^4 (V_{21}^*) \Omega^2 M_{21} - 14 m r_0^4 (V_{23}^*) \Omega^2 M_{23} - 240 e r_0^2 (U_7^*)(U_{21}^*) M_7 M_{21} - 56 e r_0^2 (U_7^*)(U_{23}^*) M_7 M_{23}]}{m^2 r_0^8 \Omega^2},$$
(14)

$$\alpha_5 = \frac{e\left[32er_0^2\left(U_{14}^*\right)^2 M_{14}^2 - 18er_0^2\left(U_{13}^*\right)^2 M_{13}^2 + 6er_0^2\left(U_{13}^*\right)\left(U_{15}^*\right)M_{13}M_{15} + 21er_0^2 M_8 M_{22}\left(U_8^*\right)\left(U_{22}^*\right)\right]}{m^2 r_0^8 \Omega^2}$$
$$+ \frac{e\left[-60mr_0^4\left(V_{21}^*\right)\Omega^2 M_{21} + 14mr_0^4\left(V_{23}^*\right)\Omega^2 M_{23} - 240er_0^2\left(U_7^*\right)\left(U_{21}^*\right)M_7 M_{21} + 56er_0^2\left(U_7^*\right)\left(U_{23}^*\right)M_7 M_{23}\right]}{m^2 r_0^8 \Omega^2}, \tag{15}$$

$$\alpha_6 = \frac{e\left[6er_0^2\left(U_{13}^*\right)\left(U_{11}^*\right)M_{13}M_{11} + 14mr_0^4\left(V_{19}^*\right)\Omega^2 M_{19} + 21er_0^2\left(U_6^*\right)\left(U_{22}^*\right)M_6 M_{22}\right]}{m^2 r_0^8 \Omega^2}$$
$$+ \frac{e\left[64er_0^2\left(U_{12}^*\right)\left(U_{14}^*\right)M_{12}M_{14} + 56er_0^2\left(U_7^*\right)\left(U_{19}^*\right)M_7 M_{19} + 21er_0^2 M_8 M_{20}\left(U_8^*\right)\left(U_{20}^*\right)\right]}{m^2 r_0^8 \Omega^2}, \tag{16}$$

$$\alpha_7 = \frac{e\left[6er_0^3\left(U_{13}^*\right)\left(U_6^*\right)M_{13}M_6 + 8mr_0^5\left(V_{12}^*\right)\Omega^2 M_{12} + 32er_0^3\left(U_{12}^*\right)\left(U_7^*\right)M_{12}M_7\right]}{m^2 r_0^8 \Omega^2}, \tag{17}$$

$$\alpha_8 = \frac{e}{m^2 r_0^8 \Omega^2}\left[8mr_0^5\left(V_{14}^*\right)\Omega^2 M_{14} + 32er_0^3\left(U_{14}^*\right)\left(U_7^*\right)M_{14}M_7 \right.$$
$$\left. + 6er_0^3 M_8 M_{13}\left(U_8^*\right)\left(U_{13}^*\right)\right], \tag{18}$$

with $\quad \omega_{0z}^2 = e\left[8er_0^4\left(U_7^*\right)^2 M_7^2 + 4mr_0^6\left(V_7^*\right)\Omega^2 M_7\right]/m^2 r_0^8 \Omega^2$, and the scaling factor $r_0$ (see definition in [24]).

## Appendix 2: Details of the steady-state solution Eq. (5)

Equation (5) is obtained by the standard steps of the multiple-scale method. Starting from Eq. (4), we assume that the driving frequency is a perturbative expansion of harmonic oscillator frequency [28], i.e., $\omega_z = \omega_{0z} + \epsilon^2 \sigma$, with a small dimensionless parameter $\epsilon$. Following the method in [29], we rewrite Eq. (4) by setting $z = \epsilon u$, $x = \epsilon p$, $y = \epsilon q$, the damping term as $2\epsilon^3 \mu \dot{u}$ and the driving term as $\epsilon^3 k_z \cos(\omega_z t)$. Introducing a new parameter $T_i = \epsilon^i t (i = 0, 1, 2)$, we rewrite $u$, $p$, $q$ as,

$$u = \epsilon^0 u_0(T_0, T_1, T_2) + \epsilon^1 u_1(T_0, T_1, T_2) + \epsilon^2 u_2(T_0, T_1, T_2),$$
$$p = \epsilon^0 p_0(T_0, T_1, T_2) + \epsilon^1 p_1(T_0, T_1, T_2) + \epsilon^2 p_2(T_0, T_1, T_2),$$
$$q = \epsilon^0 q_0(T_0, T_1, T_2) + \epsilon^1 q_1(T_0, T_1, T_2) + \epsilon^2 q_2(T_0, T_1, T_2). \tag{19}$$

Then we compare the coefficients of $\epsilon^0$, $\epsilon^1$ and $\epsilon^2$, which yields,

$$D_0^2 u_0 + \omega_{0z}^2 u_0 = 0, \tag{20}$$
$$D_0^2 u_1 + \omega_{0z}^2 u_1 = -2D_0 D_1 u_0 - \alpha_2 u_0^2 - \alpha_7 q_0 u_0 - \alpha_8 p_0 u_0, \tag{21}$$

$$D_0^2 u_2 + \omega_{0z}^2 u_2 = -[-k_z \cos(\omega_{0z} T_0 + \sigma T_2)$$
$$+ q_0^2 \alpha_4 u_0 + p_0^2 \alpha_5 u_0 + p_0 q_0 \alpha_6 u_0 + 2\mu D_0 u_0$$
$$+ D_1^2 u_0 + 2D_0 D_2 u_0 + q_0 \alpha_{21} u_0^2 + p_0 \alpha_{22} u_0^2$$
$$+ \alpha_3 u_0^3 + 2D_0 D_1 u_1 + \alpha_7 q_0 u_1 + \alpha_8 p_0 u_1$$
$$+ 2\alpha_2 u_0 u_1 + \alpha_7 q_1 u_0 + \alpha_8 p_1 u_0], \tag{22}$$

where $D_i = \partial/\partial T_i, (i = 0, 1, 2)$.

Hence, we may solve $u_0 = A(T_2)\exp(i\omega_{0z}T_0) + \bar{A}(T_2)\exp(-i\omega_{0z}T_0)$ and $u_1 = \alpha_2[A^2\exp(2i\omega_{0z}T_0) - 6A\bar{A} + \bar{A}^2\exp(-2i\omega_{0z}T_0)]/3\omega_{0z}^2$ from Eqs. (20) and (21) by eliminating the secular term. Similarly, from equations of the oscillations in $x$ axis and $y$ axis, which are similar to Eq. (4) but without the driven term, we may solve the variables $p_0, q_0, p_1$ and $q_1$ as

$$p_0 = C(T_2)\exp(i\omega_{0x}T_0) + \bar{C}(T_2)\exp(-i\omega_{0x}T_0), \tag{23}$$

$$q_0 = B(T_2)\exp(i\omega_{0y}T_0) + \bar{B}(T_2)\exp(-i\omega_{0y}T_0), \tag{24}$$

$$p_1 = \alpha_{2x}[C^2\exp(2i\omega_{0x}T_0) - 6C\bar{C} + \bar{C}^2\exp(-2i\omega_{0x}T_0)]/(3\omega_{0x}^2), \tag{25}$$

$$q_1 = \alpha_{2y}[B^2\exp(2i\omega_{0y}T_0) - 6B\bar{B} + \bar{B}^2\exp(-2i\omega_{0y}T_0)]/(3\omega_{0y}^2), \tag{26}$$

where $\alpha_{2x}$ and $\alpha_{2y}$ correspond to the quadric nonlinearity of the ion motion equation in $x$ and $y$ directions, respectively. $\omega_{0x}/2\pi$ and $\omega_{0y}/2\pi$ represent the harmonic frequencies in $x$ direction and $y$ direction. $A = \frac{1}{2}a\exp(i\beta)$, $B = \frac{1}{2}b\exp(i\varsigma)$ and $C = \frac{1}{2}c\exp(i\eta)$, where $a, b, c, \beta, \varsigma$ and $\eta$ are real functions of $T_2$, $\beta, \varsigma$ and $\eta$ represent the phases of different dimensions. $\bar{A}, \bar{B}$ and $\bar{C}$ are conjugate terms of

$A$, $B$ and $C$. Substituting $u_0$ and $u_1$ into Eq. (22), we obtain an equation regarding the secular term, from which, in combination with Eqs. (23–26) with the expressions of $A$, $B$ and $C$, we obtain

$$-\frac{1}{2}k_z \sin \gamma + a\mu\omega_{0z} + \omega_{0z}\frac{da}{dT_2} = 0, \qquad (27)$$

$$\frac{1}{2}k_z \cos \gamma - \frac{3\alpha_3 a^3}{8} - \frac{1}{4}\alpha_4 ab^2 - \frac{1}{4}\alpha_5 ac^2 + \frac{5\alpha_2^2 a^3}{12\omega_{0z}^2} + \frac{\alpha_8 \alpha_{2x} ac^2}{4\omega_{0x}^2}$$
$$+ \frac{\alpha_7 \alpha_{2y} ab^2}{4\omega_{0y}^2} + a\omega_{0z}\left(\sigma - \frac{d\gamma}{dT_2}\right)$$
$$= 0, \qquad\qquad\qquad\qquad\qquad\qquad\qquad\qquad (28)$$

with $\gamma = \sigma T_2 - \beta$. We assume the steady-state motion corresponding to $\frac{d\gamma}{dT_2} = \frac{da}{dT_2} = 0$. So we have

$$\left(\frac{3\alpha_3}{8}a^3 - \frac{5\alpha_2^2}{12\omega_{0z}^2}a^3 + \frac{\alpha_4}{4}ab^2 + \frac{\alpha_5}{4}ac^2 - \frac{\alpha_7 \alpha_{2y}}{4\omega_{0y}^2}ab^2 \right.$$
$$\left. - \frac{\alpha_8 \alpha_{2z}}{4\omega_{0x}^2}ac^2 - a\omega_{0z}\sigma\right)^2 + (a\omega_{0z}\mu)^2 = \frac{1}{4}k_z^2. \qquad (29)$$

which is actually Eq. (5).

## References

1. A.H. Nayfeh, D.T. Mook, *Nonlinear Oscillations* (Wiley-Interscience, New York, 1979)
2. M.I. Dykman, M.A. Krivoglaz, *Soviet Scientific Reviews Volume* (Harwood Academic, New York, 1984) pp. 265
3. L.D. Landau, E.M. Lifshitz, *Mechanics*, 3rd edn. (Pergamon, New York, 1976)
4. A.H. Nayfeh, *Introduction to Perturbation Techniques*. (Wiley, New York, 1981)
5. V.I. Arnold, *Geometrical Methods in the Theroy of Ordinaty Differential Equations, Volume 250 of Grundlehren der mathematischen Wissenschaften*, 2nd edn. (Springer, New York, 1988)
6. S.H. Strogatz, *Nonlinear Dynamics and Chaos: with Applications to Physics, Biology, Chemistry, and Engineering* (Perseus Books, New York City, 1994)
7. H.B. Chan, M.I. Dykman, C. Stambaugh, Phys. Rev. Lett. **100**, 130602 (2008)
8. M.I. Dykman, B. Golding, D. Ryvkine, Phys. Rev. Lett. **92**, 080602 (2004)
9. B. Yurke, E. Buks, J. Lightwave Tech. **24**, 5054 (2006)
10. E. Buks, B. Yurke, Phys. Rev. A **73**, 23815 (2006)
11. D. Leibfried, R. Blatt, C. Monroe, D. Wineland, Rev. Mod. Phys. **75**, 281 (2003)
12. W. Paul, Rev. Mod. Phys. **62**, 531 (1990)
13. N. Akerman, S. Kotler, Y. Glickman, Y. Dallal, A. Keselman, R. Ozeri, Phys. Rev. A **82**, 061402(R) (2010)
14. A.A. Makarov, Anal. Chem. **68**, 4257 (1996)
15. A. Drakoudis, M. Söllner, G. Werth, Int. J. Mass. Spectrom. **252**, 61 (2006)
16. K. Vahala, M. Herrmann, S. Knünz, V. Batteiger, G. Saathoff, T.W. Hünsch, Th. Udem, Nat. Phys. **5**, 682 (2009)
17. S. Knünz, M. Herrmann, V. Batteiger, G. Saathoff, T.W. Hünsch, K. Vahala, Th. Udem, Phys. Rev. Lett. **105**, 013004 (2010)
18. D. Kielpinksi, C. Monroe, D.J. Wineland, Nature (London) **417**, 709 (2002)
19. J.H. Wesenberg, Phys. Rev. A **78**, 063410 (2008)
20. M.G. House, Phys. Rev. A **78**, 033402 (2008)
21. R. Bradford Blakestad, *Transport of Trapped-Ion Qubits Within a Scalable Quantum Processor [D]* (California Institute of Technology, Pasadena, 2002)
22. L. Chen, W. Wan, Y. Xie, H.-Y. Wu, F. Zhou, M. Feng, Chin. Phys. Lett. **30**, 013702 (2013)
23. D.T.C. Allcock, J.A. Sherman, D.N. Stacey, A.H. Burrell, M.J. Curtis, G. Imreh, N.M. Linke, D.J. Szwer, S.C. Webster, A.M. Steane, D.M. Lucas, New J. Phys. **12**, 053026 (2010)
24. G. Littich, *Electrostatic Control and Transport of Ions on a Planar Trap for Quantum Information Processing* (ETH Zürich and University of California, Berkeley, 2011)
25. A. Doroudi, Phys. Rev. E **80**, 056603 (2009)
26. S. Sevugarajan, A.G. Menon, Int. J. Mass Spectrom. **209**, 209 (2001)
27. M. Vedel, J. Rocher, M. Knoop, F. Vedel, Appl. Phys. B **66**, 191 (1998)
28. A.H. Nayfeh, *Problems in Perturbation* (Wiley-Interscience, New York, 1985)
29. A.H. Nayfeh, J. Sound Vib. **92**, 363 (1984)